Hindawi
Shock and Vibration
Volume 2019, Article ID 4802740, 19 pages
https://doi.org/10.1155/2019/4802740

Research Article

Dynamic Failure Mode and Dynamic Response of High Slope Using Shaking Table Test

Zhijun Zhou,[1] **Chenning Ren**,[1] **Guanjun Xu**,[1] **Haochen Zhan**,[1] **and Tong Liu**[2]

[1]*School of Highway, Chang'an University, Xi'an, Shaanxi 710064, China*
[2]*School of Science, Xi'an University of Architecture and Technology, Xi'an, Shaanxi 710055, China*

Correspondence should be addressed to Tong Liu; liutong@xauat.edu.cn

Received 3 November 2018; Accepted 29 January 2019; Published 25 March 2019

Academic Editor: Filippo Santucci de Magistris

A shaking table test was performed to study the dynamic response and failure modes of high slope. Test results show that PGA amplification coefficients increased with increasing elevation and the PGA amplification coefficient of the concave slope was slightly larger than that of the convex slope. The slope type affected the dynamic response of the slope. The elevation amplification effect of the concave slope under seismic load was more significant than that of the convex slope; thus, the concave slope was more unstable than the convex slope. Additionally, the PGA amplification coefficient measured on the slope surface was always larger than that inside the slope, and the data show an increasing trend with the broken line. The dynamic amplification effect of the high slope was closely related to the natural frequency of the slope. Within a certain range, the higher the frequency, the more significant the amplification effect. The dynamic failure process of concave and convex slopes was studied through tests. Findings indicate that the dynamic failure modes of the concave slope are characterized by shoulder collapse, formation of the sliding surface, and integral sliding above the slope line. Dynamic failure modes of the convex slope are mainly slips in the soil layer and collapse of the slope near the slope line.

1. Introduction

Southwest China is an earthquake-prone area, especially in Yunnan Province, a province with high earthquake occurrence. Red beds, a rock mass with poor engineering characteristics such as low strength, poor permeability, and easy weathering, are widely distributed in Yunnan. The area hosts typical landslide-prone strata. Earthquake landslides have become the most common geological hazard in the construction of these areas [1–4]. Earthquake landslides are extremely dangerous and have caused severe casualties and property losses worldwide. In 2008, an 8.0-magnitude earthquake struck Wenchuan County, Sichuan Province, China, triggering massive slope damage, including more than 56,000 landslides resulting in 256 barrier lakes and nearly 20,000 deaths [5–8]. The Yushu earthquake in China in 2010 triggered more than 2,000 landslides with a total area of 1.194 square kilometers [9]. On July 22, 2013, a magnitude 5.9 earthquake occurred in Minxian, China, which also triggered more than 2,000 slope damages [10]. Therefore, slope stability has become a prominent technical problem in the construction of southwest Yunnan.

The dynamic stability of slopes is an important topic in geotechnical engineering [11]. The study of slope dynamic response law is the foundation of slope dynamic stability analysis, including responses of acceleration, velocity, displacement, and stress-strain equivalents [12, 13]. Accurate understanding of the dynamic response characteristics of slopes under seismic loads can provide scientific and theoretical guidance for seismic designs in slope engineering.

Methods for studying seismic responses of slopes mainly include numerical simulation and model testing. The numerical calculation method can simulate the actual failure mechanism of landslides [14, 15]. Toki et al. used the finite element method to conduct slope dynamic stability analysis [16]. Jiang et al. employed numerical methods to study the dynamic failure process of the model [17]. However, some simple numerical values or correction coefficients cannot be used to accurately simulate actual situations due to the complexity of projects, leading to deviations in experimental

conclusions. In recent years, researchers have begun to use the shaking table model test to study dynamic slope response. This test system can reproduce earthquake excitation and collect test data automatically and accurately. Therefore, the shaking table test is a direct method used to reveal structural dynamic response and failure modes; the approach has been widely used in seismic response research on various structures [18–20].

Clough and Pirtz carried out a preliminary shaking table test study on the stability of slopes under earthquake conditions [21]. Wang and Zhang used a vibration simulation test to study the dynamic stability of a rock slope [22]. Wang and Lin used a shaking table test to analyze the initiation and displacement of landslides under earthquakes [23]. Yang et al. investigated the disaster phenomenon of the Wenchuan earthquake landslide based on a shaking table test [24]. Zhao et al. examined the mechanisms of deformation and instability of seismic slopes via a shaking table test [25]. Matsuo used a large shaking table to study the dynamic response and failure modes of a geosynthetics-reinforced earth retaining wall [26]. Through a large-scale shaking table test, Xu et al. studied the dynamic response law of a slope [27]. Yang et al. investigated the dynamic failure mechanism and dynamic response characteristics of a counter-bedding slope under earthquake excitation [28]. Che et al. used a shaking table test to analyze the influence of discontinuous joints on a high and steep slope in an earthquake [29]. Lee et al. used shaking table model tests to study seismic dynamic response characteristics of dry sand and saturated sedimentary sand; they also discussed the boundary effect of the layered model box [30]. Based on energy dissipation theory, Kokusho and Ishizawa studied the failure mechanism of slopes under seismic loads using a small-scale shaking table test, and the Newmark method was employed to calculate and analyze the failure mechanism [31]. Ling et al. introduced a high-rise concrete model with a 2.7-meter-thick transfer slab into seismic action representing small, medium, and large earthquakes [32]. Wartman et al. carried out a physical model experiment with a 1 g shaking table [33]. Lin and Wang studied the dynamic response of slopes excited by sinusoidal waves (loading frequency of 8.9 Hz) using homogeneous sandy soil (water content of 5.1%) model slopes. Results showed that the slopes exhibited elastic characteristics when the acceleration amplitude was less than 0.4 g, and the amplification effect of slopes was significant as the nonlinear characteristics of soil became stronger [34].

Based on a field investigation of typical high slopes in southwestern Yunnan, we summarized the failure mechanism of model slopes via a shaking table test. On the basis of measured data, the effects of landform, slope type, elevation, and ground motion parameters on the dynamic response of the slope were analyzed in detail.

2. Study Area

Dabao and Baolong expressways are located in the red bed area of Yunnan province (Figure 1). The lithology of the red bed soft rock area is mainly composed of mudstone and sandstone; some rocks are complex lithologic assemblages formed by the interbedding of hard and soft rocks. Basic characteristics of slope height, slope morphology, and lithology combination were obtained through field investigation.

An investigation of 97 slopes along the Dabao and Baolong expressways revealed many high rock slopes, 80% of which exceeded 20 m and many of which were irregularly shaped. There are a few types of convex and concave slopes: the upper part of the concave slope is steep, and the lower part is gentle, while the slope is protected by anchor frame beams; the upper part of the convex slope is gentle and the lower part is almost vertical, and the rock surface is weathered.

Figure 2 presents a common lithology combination diagram of soft and hard interbedded slopes. The upper part and surface of the rock mass are weathered and exhibit a vegetation layer, and two muddy interlayers exist inside the slope. These muddy interlayers formed under various geological tectonic action and long-term groundwater action. The weak interlayer plays a vital role in controlling slope stability.

3. Experimental Method

3.1. Test Device. The shaking table test was conducted in the Key Laboratory of Structural Engineering and Seismic Resistance, Ministry of Education, Xi'an University of Architecture and Technology, China. A unidirectional two-degrees-of-freedom shaking table (Figure 3) was adopted in the experiment. The platform size measured 2.2×2 m with a maximum load capacity of 40 tons. The maximum acceleration at full load was $\pm 27.7\ \mathrm{m \cdot s^{-2}}$, and the working frequency range was 0.01–30 Hz; specific parameters are listed in Table 1.

A rigid model box with an internal size of 1.84 m × 1.3 m × 1.1 m was adopted in this test, welded from a steel plate and angle steel. The rigid model box was constructed of plexiglass on both sides to allow for observation of the slope failure process during vibration. The model box was lined with a 5 cm thick foam cushion on the back wall to reduce the boundary effect of the box. This method to reduce the model box effect has been adopted by many scholars [35, 36]. A wooden baffle was fixed in the center of the model box with angle steel and bolts and used to separate the two models. The baffle was made of waterproof and smooth wooden materials.

3.2. Test Model. The experimental model did not correspond fully to the characteristics of the high rock slope in southwestern Yunnan; rather, the model was simplified and manufactured according to common characteristics of slopes in this area. Two slope models (concave and convex) were included in this experiment. The scale of each model was 1 : 30; the height of each model was 1 m, the width of the top of the slope was 0.4 m, and the width of the bottom of the slope was 1.2 m. Both models adopted 1 : 0.5 and 1 : 1 slope rates. Taking barite powder, quartz sand, and gypsum as

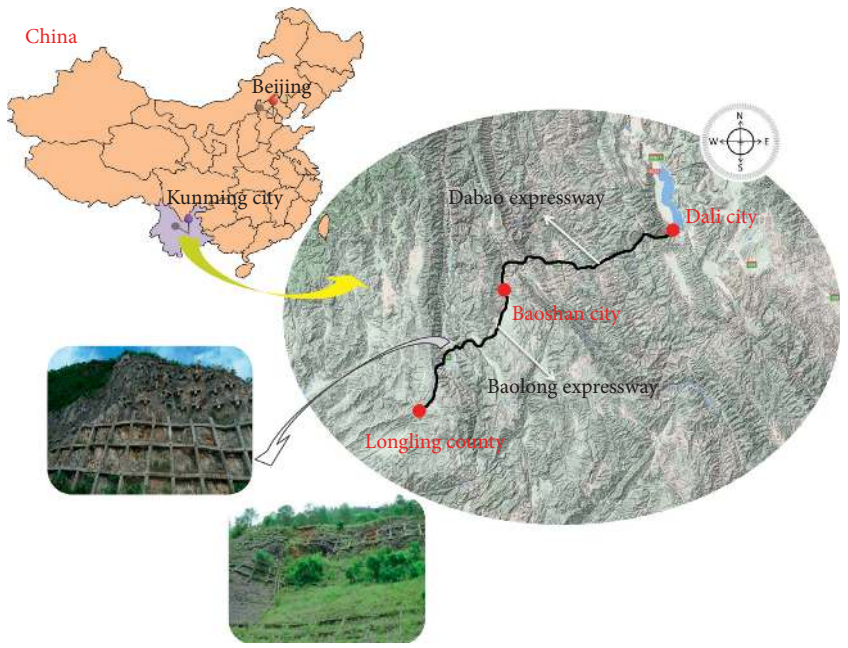

Figure 1: Location map of the study area.

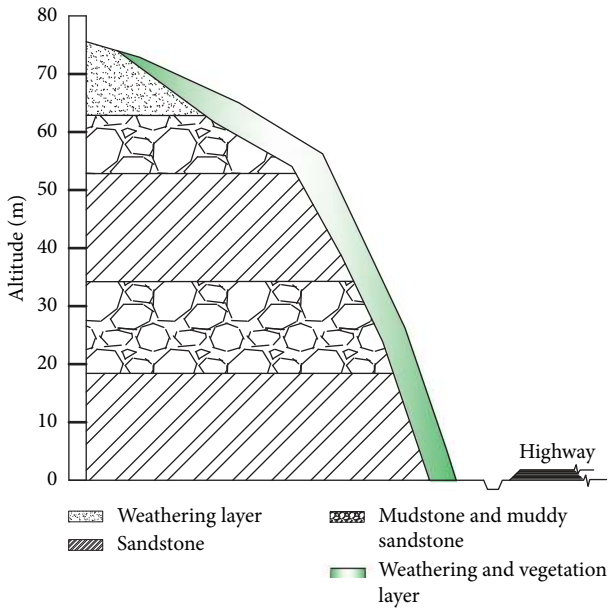

Figure 2: Typical slope profile.

aggregates, the model was built by stratified compaction according to the ratio of 32 : 56 : 9 by controlling water content. Four layers of a muddy interlayer interface (made of clay) were included with a thickness of 2 cm in the model slope, placed 0.2 m, 0.5 m, 0.7 m, and 0.9 m away from the bottom of the box, respectively. The height of the bottom step was 15 cm, which was paved and compacted on the bottom of the box to increase model stability. Concave and convex slopes were placed in the same model box, separated by partitions and subjected to the same input motion. Figure 4 shows the completed models and the key steps of model construction.

Model construction is inherently complicated, and every step should be precise. The model-making process in this paper involved the following steps:

(1) Proportionally mixed model materials were packed into the model box in batches, with 10 cm as a layer and then filled and compacted in layers. The boundary of each compacted layer was marked with vermilion-colored sand so model deformation and settlement could be observed through plexiglass on the side of the model box.

(2) When compacted to the interface of the designed weak interlayer, a layer of clay with a thickness of 2 cm was laid on the compacted surface, and the side was marked with blue sand. According to the design, four layers of clay were spread during compaction.

(3) In the model-making process, the sensor was buried in the design position and small red plastic particles were sprayed on the upper surface; thus, the sensor could be easily found without damage when removing the model.

(4) The slope surface was cut to make the shape coincide with the designed slope shape.

3.3. Similarity Relation and Similar Materials. Based on π theorem [37–39], the similarity criterion was derived through dimensional analysis. Because of the complexity of the model, it would be difficult to meet similarity of all parameters. It was thus necessary to select the main control parameters as fundamental dimensions according to the test purpose and model characteristics. This test took geometric length, density, and acceleration as fundamental dimensions; similar constants of the test appear in Table 2.

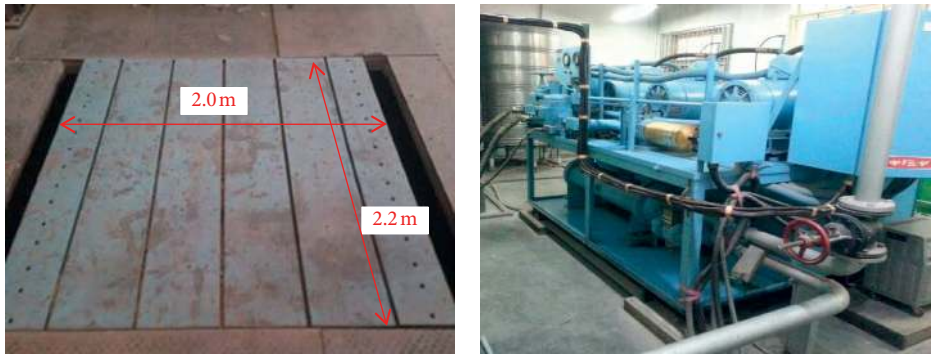

(a) (b)

Figure 3: Shaking table system. (a) Shaking table surface. (b) Dynamic system of shaking table.

Table 1: Technical parameters of shaking table.

Technical parameters	Value	Technical parameters	Value
Platform size (m)	2.2 × 2	Vibrate wave type	Sine wave, El Centro wave
Maximum specimen weight (KN)	40	Maximum acceleration (m/s^2)	±27.7
Frequency (Hz)	0.01~30	Maximum amplitude (mm)	±100

(a) (b) (c) (d) (e)

Figure 4: Photos of completed models and the key steps of model construction. (a) View 1 of finished models. (b) View 2 of finished models. (c) Laying of muddy interlayer interface. (d) Compaction of model. (e) Cutting ring method.

Although many materials could be used for modeling, we could not identify an ideally similar material. Therefore, it is essential to understand the properties of test materials. Similar materials should meet the requirements of low price, stable mechanical properties, easy formation, simple measurement, uniformity, and isotropy. Similar materials generally consist of aggregates, cementing agents, and auxiliary materials in certain proportions. Barite powder

Table 2: The similarity ratios of the test model.

Parameters	Similarity relation	Similarity constant
Physical dimension (L)	C_L	30*
Density (ρ)	C_ρ	1*
Shear modulus (G)	$C_G = C_L C_\rho C_a$	30
Poisson's ratio (μ)	C_μ	1
Cohesion (c)	$C_c = C_L C_\rho C_a$	30
Internal friction angle (φ)	C_φ	1
Acceleration (a)	C_a	1*
Acceleration of gravity (g)	$C_g = C_a$	1
Frequency (ω)	$C_\omega = C_a^{1/2}/C_L^{1/2}$	0.18
Stress (σ)	$C_\sigma = C_L C_\rho C_a$	30
Strain (ε)	$C_\varepsilon = 1$	1
Time (t)	$C_t = C_L^{1/2}/C_a^{1/2}$	5.48
Displacement (s)	$C_s = C_L$	30
Velocity (v)	$C_v = C_L^{1/2} C_a^{1/2}$	5.48

Note. L, ρ, and a are controlling parameters. *Fundamental dimensions.

Table 3: Types and properties of model materials.

Category	Name	Properties and function
Aggregate	Quartz sand, barite powder	Quartz sand is used as a coarse aggregate to change the internal friction angle and adjust the compressive strength and elastic modulus of specimens. Barite powder can be used to adjust the material weight because of its high gravity
Cementing agent	Gesso	Shaped the model due to its bonding effect
Additive	Water	Controlled water content
Auxiliary materials	Clay	Simulated mudstone muddy weak interlayer structure plane

and quartz sand were selected in this study as coarse aggregates along with gypsum as the cementing agent and water as an additive. Clay was chosen to simulate the interface of the weak interlayer. The physical and chemical properties of aggregates were stable, and the barite powder was of great weight, thus meeting material requirements discussed above. Properties of similar materials are shown in Table 3.

To obtain an appropriate material ratio, several indoor geotechnical tests were conducted to acquire the physical and mechanical parameters of mixtures with different ratios. The density of the model material was measured using a ring knife test: the model material was cut with a certain volume ring knife and weighed. The density of the material was the ratio of mass to volume of the material in the ring knife. The water content of the material was determined by a drying method: model material of a certain quality was weighed and placed into a drying oven and maintained at 105–110 degrees Celsius until the material reached a constant weight. The ratio of the lost water quality to material quality after drying represented the water content. The cohesion and internal friction angle of materials were measured using a consolidated undrained shear test; the cylindrical specimen was coated with latex film and placed in a sealed pressure chamber. The material was equalized by injection of hydraulic pressure. At the same time, the drain valve was opened to consolidate the specimen fully, after which the drain valve was closed to apply axial pressure to destroy the specimen. Experimental results were plotted as $\sigma - \tau$ curves, and values of c and ϕ were obtained. The shear modulus of materials with different ratios was measured by a dynamic triaxial test. By comparing the physical and mechanical indices of materials in different proportions, the proportioning scheme closest to the parameters of similar models was found. Finally, a 32 : 56 : 9 : 8 ratio of barite powder: quartz sand: gypsum powder: water completed the slope model. Table 4 shows the main physicomechanical parameters of mudstone and similar materials; the indoor geotechnical test is depicted in Figure 5.

3.4. Measurement System and Input Motion. A total of 18 acceleration sensors and 4 displacement sensors were used in the experiment. Accelerometers A1 to A16 were symmetrically distributed in two models as shown in Figure 6. Displacement sensors S1 and S2 were attached on the top of the slope to compare with the displacement obtained by integrating the acceleration time-history curve. Sensors A0 and A0′ and sensors S0 and S0′ were symmetrically arranged in the model; accelerometer A0′ and displacement sensor S0′ were installed on the top of the model box to monitor the dynamic response of the box. Acceleration sensor A0 and displacement sensor S0 were arranged on the shaking table surface. Acceleration sensors A15 and A16 were embedded in concave and convex slopes, respectively, 10 cm away from the box wall and 30 cm away from the bottom of the box; these sensors were used to detect the effect of the flexible boundary of the model box. Sensors A1, A7, and A13 were arranged on the same vertical line of the concave slope, 20 cm away from the box wall. Sensors A3, A9, and A14 were installed on corresponding points of the convex slope. Sensors A2, A5, A8, and A11 were arranged at elevations of 20 cm, 40 cm, 60 cm, and 80 cm, respectively, in the convex slope. Sensors A4, A6, A10, and A12 were installed at symmetrical measuring points on the convex slope. All sensors were waterproof. Figure 6 shows the full dimensions of the model slope and layout of the acceleration monitoring points.

For the loading scheme, elucidated in Table 5, the test adopted two wave patterns of an El Centro wave and sine wave with a time compression ratio of 5.48. The sine wave adopted four frequency grades: 5 Hz, 7.5 Hz, 10 Hz, and 12.5 Hz. The peak acceleration value in the test loading scheme was determined according to the corresponding relationship between seismic fortification intensity and basic acceleration of ground motion in the Code for Seismic Design of Buildings (GB50011-2010). The seismic fortification intensity in southwestern Yunnan is VII–IX. Peak acceleration levels of 0.1 g, 0.2 g, 0.3 g, and 0.4 g were designed corresponding to the fortification intensity, and the loading conditions of 0.6 g, 0.8 g, and 1.0 g were added. Considering that the sine wave was more destructive, only

Table 4: Main physicomechanical parameters of prototype and model materials.

Lithology		Density ρ (g/cm^3)	Shear modulus G (MPa)	Poisson ratio	Cohesion c (KPa)	Internal friction angle φ (°)
Red bed soft rock (mudstone)	Prototype	2.47	1900	0.3	532	24.04
Similar material	Model	2.4	63.3	0.3	17.3	24.5

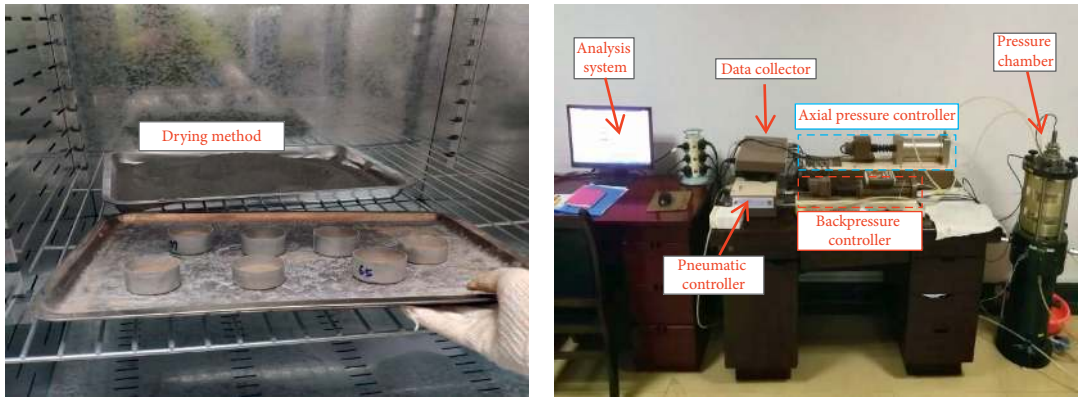

(a) (b)

Figure 5: Photos of indoor geotechnical tests. (a) Drying method. (b) Triaxial test.

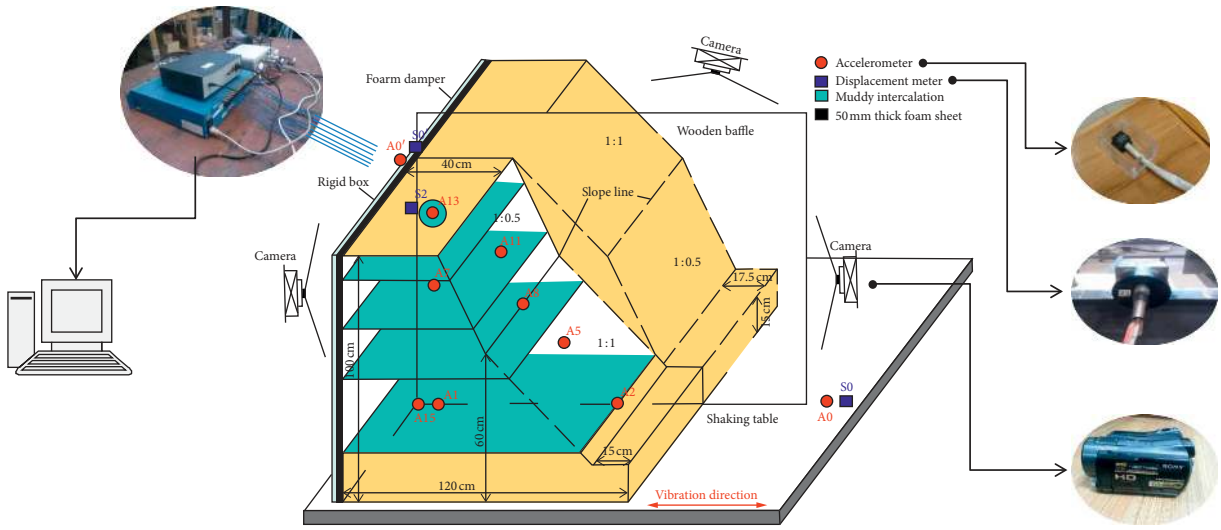

Figure 6: Full dimensions of model slope and layout of measurement points and accelerometers.

0.1 g and 0.3 g levels with different frequencies were adopted in the test.

White noise is an important means of measuring dynamic characteristics of a structure. To understand the dynamic characteristics of the model before and after excitation, white noise sweeping was applied at different stages. Model deformation was observed and recorded 15 minutes after every condition was implemented.

4. Dynamic Characteristics of Model Slope

Dynamic characteristics of the slope model included natural frequency and damping ratio. Dynamic characteristics were determined through the shaking table test, and variations in dynamic characteristics with the input seismic parameters of the platform were studied. Before the experiment was conducted, dynamic characteristics of the model box and treated boundary conditions were checked to prevent the "model box effect" from influencing the test results.

4.1. Natural Frequency Analysis of Model Box. The rigid model box used in the experiment had its own natural frequency. When the natural frequency of the model box was close to that of the input seismic wave, a resonance phenomenon occurred. The model box produced large vibration, which destroyed the stability of the model slope and affected the test accuracy.

Table 5: The test loading scheme.

No.	Earthquake record	Types of seismic waves	Peak acceleration (g)
1	WN-1	White noise	0.05
2	ELC-1	El Centro	0.10
3	SIN-1	Sine wave 5 Hz	
4	SIN-2	Sine wave 7.5 Hz	0.10
5	SIN-3	Sine wave 10 Hz	
6	SIN-4	Sine wave 12.5 Hz	
7	WN-2	White noise	0.05
8	ELC-2	El Centro	0.20
9	ELC-3	El Centro	0.30
10	WN-3	White noise	0.05
11	ELC-4	El Centro	0.40
12	ELC-5	El Centro	0.60
13	WN-4	White noise	0.05
14	SIN-5	Sine wave 5 Hz	0.30
15	SIN-6	Sine wave 7.5 Hz	
16	WN-5	White noise	0.05
17	ELC-6	El Centro	0.80
18	ELC-7	El Centro	1.00
19	WN-6	White noise	0.05
20	SIN-7	Sine wave 10 Hz	
21	SIN-8	Sine wave 12.5 Hz	0.30
22	SIN-9	Sine wave 14 Hz	
23	WN-7	White noise	0.05
24	SIN-10	Sine wave 10 Hz	
25	SIN-11	Sine wave 12.5 Hz	0.50
26	SIN-12	Sine wave 15 Hz	
27	WN-8	White noise	0.05

Remarks: (1) Microseismic tests were carried out for the models by inputting white noise at the beginning of the test to measure the dynamic characteristics of the model. (2) White noise was input into the models after loading the seismic wave to measure changes in the dynamic characteristics of the model. (3) Cross-input of two seismic waves was used to observe and compare the effects of different types of seismic waves on the model slope.

To avoid resonance between the rigid model box and the loaded seismic wave, a natural frequency experiment was carried out on the model box before the test. The natural frequency of the model box was 43.467 Hz, determined by a hammer test (Figure 7), which was much larger than the frequencies of seismic waves designed in the loading scheme and the natural frequencies of the model slope; thus, further testing avoided the resonance phenomenon.

4.2. Boundary Effect Analysis of Model Box. As a semi-infinite body, a slope has no boundary in theory. In a shaking table test, however, the model can only be placed in a container of limited size. Because seismic waves propagate in soil, a series of reflections and refractions occur on the wall of the box along with changes in the vibration form of the system, which will introduce certain errors to the test, namely, the "model box effect." Effective simulation of soil boundary conditions should cause the model in the container to deform similarly to the original model in the free field under an earthquake to reduce the influence of boundary conditions. For this reason, the boundary effect of the model box wall was treated before the test; the specific method was described above. The boundary effect was tested using special measuring points. Accelerometers A2 and A4 were compared with A0 to analyze the friction boundary effect; accelerometers A15 and A16 were compared with A1 and A3 to analyze the flexible boundary effect.

As shown in Figure 8, peak acceleration at the A2 and A4 measurement points was significantly higher than that at A0. Waveforms at the A2 and A4 measured points did not lag obviously behind that of A0, indicating that the bottom of the model and the boundary of the model box were in good contact and exhibited no relative sliding. The frictional boundary was well treated and effectively simulated boundary conditions of real slope.

Figure 9 reveals that the time-history curves were in good agreement; therefore, the flexible boundary of the model box wall was well treated in the test. The difference between peak acceleration values of two measuring points near the box wall at the same elevation point was not substantial, confirming that the flexible boundary essentially met the test requirements to reduce the influence of boundary effect of model box on test results.

4.3. Modal Parameter Analysis. Modal parameter analysis is an important part of dynamic signal processing in shaking table tests. The purpose is to determine the modal damping ratio, natural frequency, and other modal parameters from obtained signals. According to the loading scheme, white noise with 0.05 g amplitude was used to excite the slope. The frequency response function was obtained by the acceleration response time history of the measuring points. Then the dynamic characteristics of the model, such as natural frequency and damping ratio, were obtained by modal parameter identification technology.

Taking the convex slope as an example, the modal parameters of measuring points excited by white noise under various working conditions are listed in Table 6 with the variation trend illustrated in Figure 10. The natural frequencies and damping ratios of different points were identical under the same conditions, indicating that slope modal parameters were not related to elevation. As the white noise gradually increased, the first-order natural frequencies of the model exhibited a gradual decline while the damping ratios gradually increased. This phenomenon occurred because the dynamic shear strength and dynamic shear modulus of rock and soil decreased, whereas the nonlinear characteristics strengthened under vibration excitation.

5. Dynamic Response of Model Slope

The dynamic response of a slope under seismic load can be used to judge slope stability, representing an important means of predicting high-slope deformation and failure. The dynamic response of the model slope induced acceleration, velocity, and displacement. Examinations of seismic damage have revealed that seismic inertia force related to acceleration is the main cause of slope deformation and instability; many scholars thus take acceleration as the object of dynamic analysis [40–44]. This

Figure 7: Hammer test of model box.

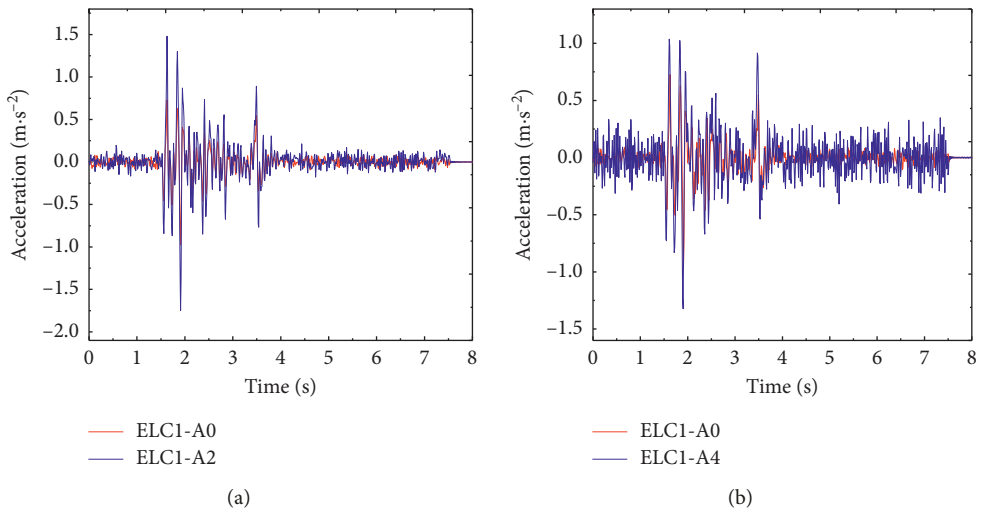

Figure 8: (a) Comparison of acceleration time-history curves between A2 and A0. (b) Comparison of acceleration time-history curves between A4 and A0.

experiment mainly studies the response laws of acceleration, velocity, and displacement of the model slope. In the test, we monitored acceleration responses of the slope from different measuring points by inputting seismic waves with different ground motion parameters. The mass and volume of displacement sensor are too large to be installed inside the slope. It could affect the failure modes of the slope and the accuracy of the test. Therefore, the sensors embedded in the model are all acceleration sensors. Velocity and displacement time-history curves were obtained by integrating acceleration time-history curves. The PGA amplification coefficient P_{AX} was selected as the index to describe the acceleration response law, defined as the ratio of the peak acceleration value of each measuring point A_X to the peak acceleration value measured on the shaking table surface A_0.

5.1. Dynamic Response of Acceleration. According to Table 7, the peak acceleration of each measuring point on the slope enlarged to varying degrees relative to the measured point on the shaking table. The acceleration amplitudes of El Centro waves were 0.1 g, 0.2 g, 0.3 g, 0.4 g, 0.6 g, 0.8 g, and 1.0 g, respectively. The acceleration amplification effect near the slope line and slope shoulder of the two models was most obvious. Taking ELC-3 as an example, the peak acceleration at the shoulder and slope line of the two slopes increased by 102% and 59% and 114% and 109% compared

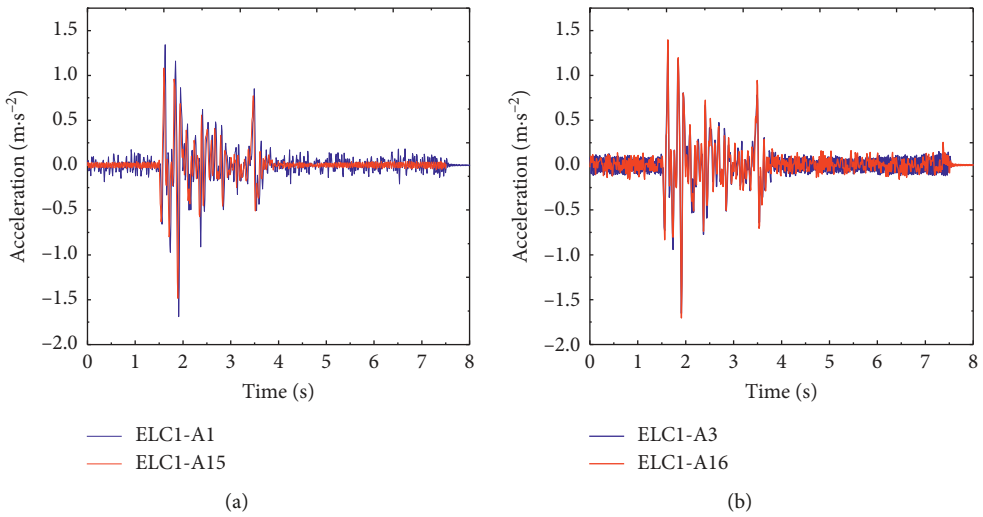

Figure 9: (a) Comparison of acceleration time-history curves between A15 and A1. (b) Comparison of acceleration time-history curves between A16 and A3.

Table 6: First-order modal parameters for convex slope internal measurement points.

Condition	A3		A9		A14		Average value	
	Frequency (Hz)	Damping ratio (%)	Frequency (Hz)	Damping ratio (%)	Frequency (Hz)	Damping ratio (%)	Frequency (Hz)	Damping ratio (%)
WN-1	16.12	9.82	16.12	9.82	16.12	9.82	16.12	9.82
WN-2	16.1	9.83	16.1	9.83	16.1	9.83	16.1	9.83
WN-3	16.0	9.84	16.0	9.84	16.0	9.84	16.0	9.84
WN-4	15.2	9.95	15.2	9.95	15.2	9.95	15.2	9.95
WN-5	14.5	10.4	14.5	10.4	14.5	10.4	14.5	10.4
WN-6	14.2	10.8	14.2	10.8	14.2	10.8	14.2	10.8
WN-7	14.1	10.9	14.1	10.9	14.1	10.9	14.1	10.9
WN-8	13.1	11.6	13.1	11.6	13.1	11.6	13.1	11.6

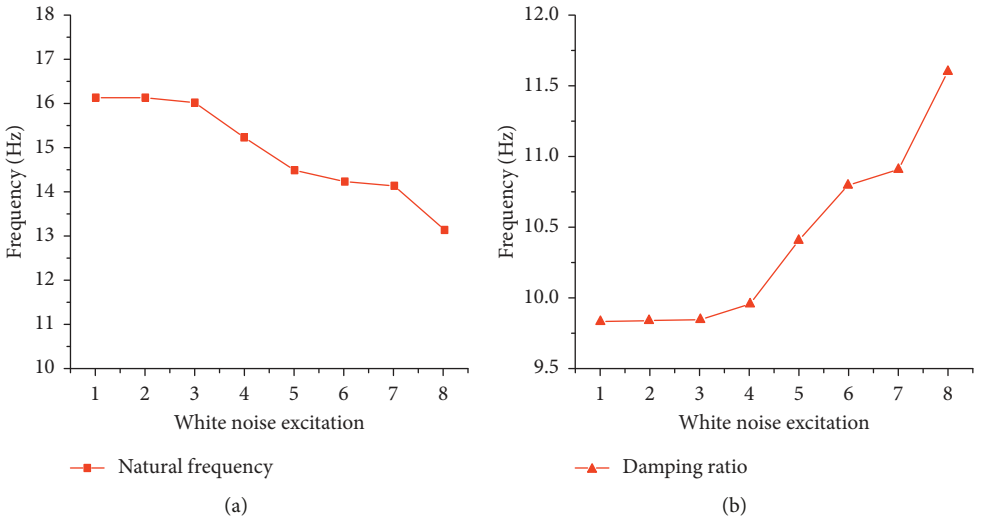

Figure 10: Variation rules of modal parameters of model.

with those measured on the shaking table, and the peak acceleration at other measuring points increased to varying degrees.

5.2. Dynamic Response of Velocity and Displacement. Like the PGA amplification coefficient, the PGV amplification coefficient and PDG amplification coefficient are defined as the

Table 7: Peak acceleration of each measuring point under El Centro waves (m/s^2).

Measuring point		Condition						
		ELC-1	ELC-2	ELC-3	ELC-4	ELC-5	ELC-6	ELC-7
Surface of shaking table	A0	1.09	2.07	3.01	4.06	6.11	7.96	10.63
Convex slope	A4	1.34	3.17	4.45	5.35	8.86	8.75	10.02
	A3	1.49	3.64	5.67	6.17	9.04	9.71	11.81
	A6	1.80	4.26	6.26	8.61	13.01	13.21	15.13
	A10	1.55	3.37	4.78	7.11	11.31	13.61	11.27
	A9	1.42	3.0	4.59	6.33	10.08	14.32	10.5
	A12	1.84	3.95	6.08	9.37	14.48	16.47	10.78
	A14	1.86	3.66	6.89	9.54	12.77	16.71	12.95
	A16	1.51	3.68	5.69	6.57	10.04	9.81	11.91
Concave slope	A2	1.53	3.79	6.37	7.83	11.73	12.25	11.92
	A1	1.51	3.77	5.98	6.57	9.83	11.14	11.84
	A5	1.85	4.03	7.16	8.81	13.62	16.71	12.92
	A8	1.63	3.87	6.30	7.31	10.94	14.56	13.66
	A7	1.5	3.33	5.41	6.94	10.45	15.2	11.69
	A11	1.68	4.16	6.44	9.25	13.44	17.67	9.21
	A13	1.88	3.89	7.19	9.21	14.05	17.03	11.52
	A15	1.53	3.97	5.78	6.67	9.78	11.67	11.21

ratio of a certain measured point value in the model to the measured point value on the platform. Taking ELC-3 as an example, the PGV and PGD amplification coefficients of the slope shoulder, slope line, and slope toe were obtained by analyzing the velocity and displacement time-history curves. According to Figure 11, the PGV amplification coefficient measured on the convex slope shoulder was 1.72 whereas those measured on the slope line and slope toe were between 1.2 and 1.6. The PGV amplification coefficient measured on the concave slope shoulder was 1.81, and those measured on the slope line and slope toe were approximately 1.5. The velocity dynamic response on the two slopes was remarkable. The PGD amplification coefficient of the convex and concave slopes from toe to shoulder showed an increasing trend. Coefficients of the convex and concave slope were 1.25 and 1.29, respectively. These findings suggest that the PGV and PGD amplification effects of the two slopes were each significant. The velocity and displacement magnification effect of the concave slope was clearly stronger than that of the convex slope.

Due to the error of the test equipment itself, the accuracy of displacement values obtained by integration needs to be verified by displacement sensor S1 and S2. Taking ELC-1 as an example, by analyzing the displacement time-history curve obtained by displacement sensor, the displacement peak value of sensor S1 on convex slope is 1.35 mm and that of sensor S2 on concave slope is 1.40 mm. The displacement peak values obtained by integration at the shoulder of concave and convex slopes are 1.36 mm and 1.41 mm, respectively (since there is no acceleration sensors at the top of the slope, the data of acceleration sensor at the shoulder nearest to the slope top were used). By comparison, it can be found that the displacement peak values obtained by displacement sensors are little different from those obtained by integration. Therefore, the instantaneous displacement peak values integrated by acceleration time-history curve can be used as the maximum displacement value of slope [45–47].

5.3. Influencing Factors of Dynamic Response of High Slope. The dynamic response of a high slope under seismic load is closely related to the geometric parameters of the slope, mechanical parameters of the soil, and seismic load parameters. Studying the influences of various parameters on the dynamic response of the slope can further reveal the failure mechanism of slope instability. In this experiment, a set of rock slope models with different slope shapes was designed, and four layers of weak interlayer structural planes were designed inside the slope to ensure the model structure approximated the high slope in southwestern Yunnan. Acceleration data and the effects of slope shape, landforms, elevation, and seismic parameters on the dynamic response of acceleration were examined.

Taking ELC-3 and SIN-1 as examples (Figure 12), similarities were identified between the two slope models: PGA amplification coefficients of the convex and concave slopes exhibited an overall upward trend along the elevation with a broken line. The PGA amplification coefficients of the two slopes declined sharply near the slope line, especially at the measuring points (40 cm high) below the slope line. The PGA amplification coefficients of the slopes rose sharply at the slope shoulder, which was substantially higher than the other points. In terms of differences, the PGA amplification coefficients measured at each point on the concave slope were slightly larger than those on the convex slope, especially measured above the slope line. The amplification effect on the concave slope shoulder (80 cm high) was more obvious than that on the concave slope; therefore, the concave slope shoulder sustained damage before the convex slope.

The influences of topography and elevation on the dynamic response of slopes under seismic loads have been studied extensively. Regarding landforms, the slope surface is controlled by factors such as the free surface; the magnification effect differs from that of the rock mass in the slope in the horizontal direction. The effect of elevation is due to the elevation amplification effect.

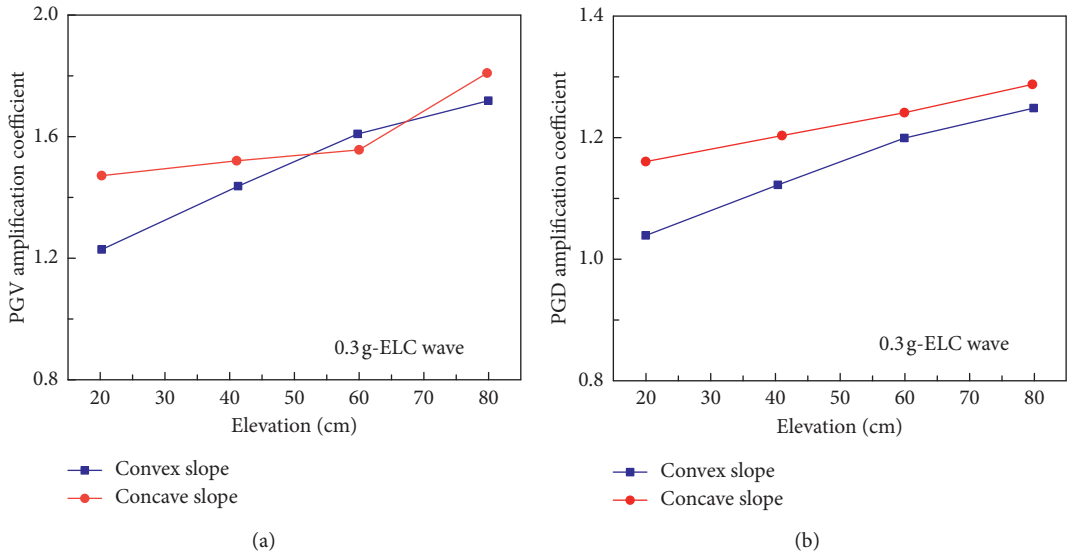

Figure 11: Variation curves of (a) PGV and (b) PGD amplification coefficient.

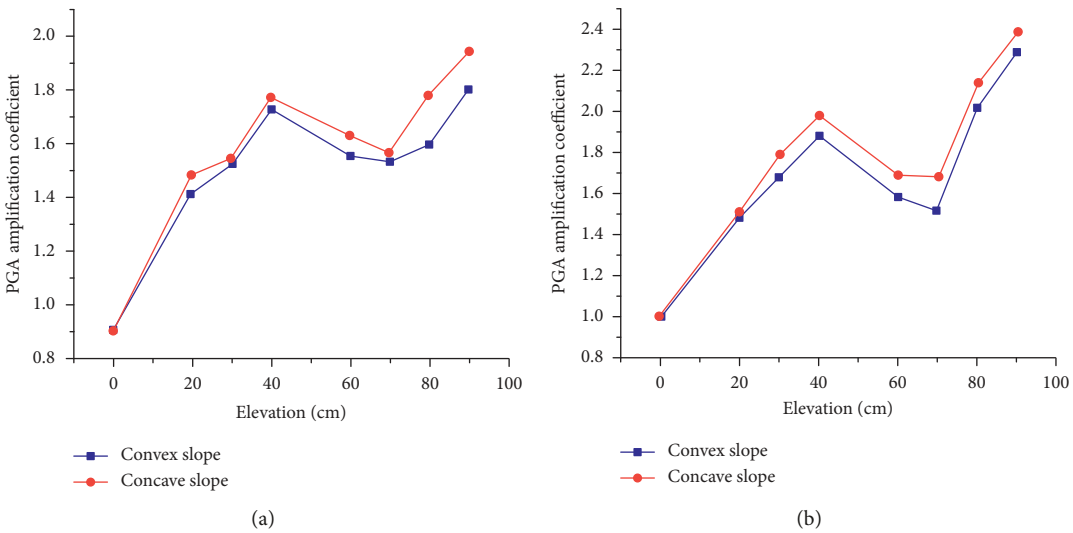

Figure 12: PGA amplification coefficients under (a) SIN-1 and (b) ELC-3.

Taking ELC-1 and SIN-1 as examples, the curve of PGA amplification coefficients varied with elevation. Figure 13 shows that the PGA amplification coefficients measured on both slope surfaces were significantly larger than those inside the slopes, and the difference was larger near the slope line at the same elevation. The gap narrowed gradually with an increase in elevation, and the two curves essentially retained a parallel upward trend. Under the ELC-1 condition, PGA amplification coefficients measured inside the slope below the slope line of the convex slope largely remained within 1.5. The amplification effect was more obvious near the slope shoulder, with coefficients close to 1.8 exhibiting a sharp upward trend. The PGA amplification coefficients measured on the slope surface exceeded 1.8 near the slope line, which demonstrated an initial downward trend followed by a dramatic increase near the line. All PGA amplification coefficients measured on the concave slope surface were greater than those inside the concave slope. Acceleration amplification peaked near the concave slope shoulder, with PGA amplification coefficients reaching approximately 2.0.

Figure 14 depicts the curve of PGA amplification coefficients along elevation under the SIN-1. Results show that amplification effect of convex slope surface was remarkable in the horizontal direction, and PGA amplification coefficients at each elevation point were greater than those inside the slope. Two curves grew in broken lines, exhibiting nonlinear characteristics, and the PGA amplification coefficients changed markedly at the slope line and slope shoulder.

Measuring points on the slope surface were not in the same vertical direction, hence three measuring points inside

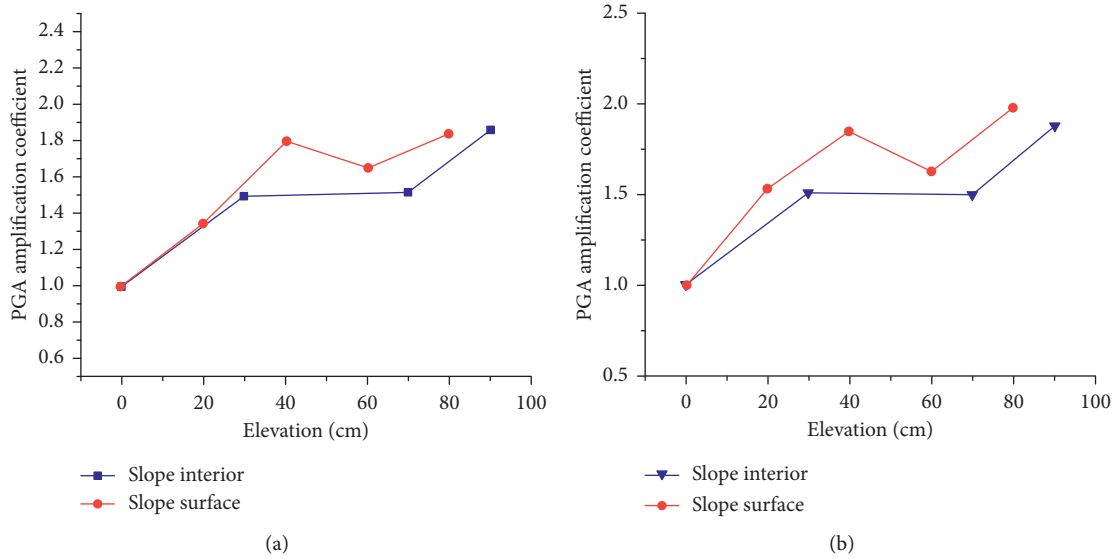

Figure 13: PGA amplification coefficients under condition ELC-1. (a) Convex slope. (b) Concave slope.

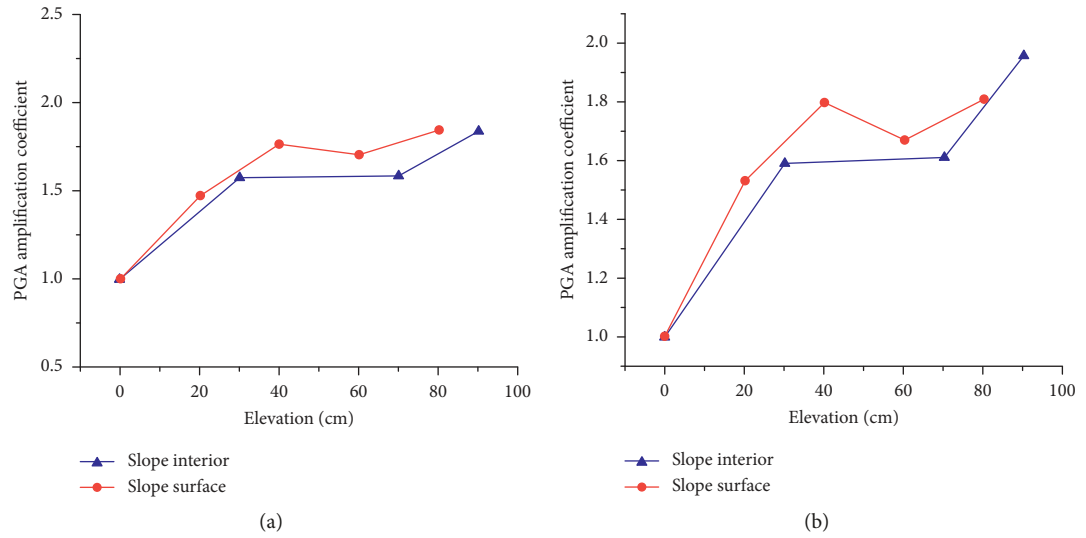

Figure 14: PGA amplification coefficients under condition SIN-1. (a) Convex slope. (b) Concave slope.

the slope being selected as objects for analysis. Taking ELC-1 and SIN-1 as examples (Figure 15), the PGA amplification coefficients increased in line with elevation; they declined near the slope line under certain conditions. The influences of slope type, a weak interlayer, and ground motion parameters caused the magnification effect along the elevation to show an upward trend and minor reduction at certain positions. These findings indicate that the magnification effect of the concave slope was more significant.

Slope dynamic response is closely related to seismic characteristics of the slope, including the seismic wave type, seismic amplitude, frequency, and other characteristics. The experiment included two kinds of seismic wave input, an El Centro wave and sine wave, and took ELC-1 and SIN-1 as examples (Figure 16). The PGA amplification coefficients corresponding to A4, A6, and A12 under SIN-1 were obviously larger than those under ELC-1. The acceleration amplification effect therefore differed under varying seismic waves, potentially due to the distinct spectral characteristics of different seismic waves.

Two loading schemes were designed for seismic waves. Under an El Centro wave, the acceleration amplitudes were divided into 6 grades: 0.1 g, 0.2 g, 0.3 g, 0.4 g, 0.6 g, and 0.8 g. Under a sine wave, the acceleration amplitudes were 0.1 g and 0.3 g. As indicated in Figures 17 and 18, PGA amplification coefficients showed an increasing trend at small amplitudes (0.1 g–0.3 g), remained stable between 0.4 g and 0.6 g, and then declined once the amplitude exceeded 0.6 g. The PGA amplification coefficients of A3 exhibited an initial increase from 0.1 g to 0.3 g followed by a decline, and the range was wider. A9 and A14 increased initially followed by a stable stage and finally fell. The PGA amplification

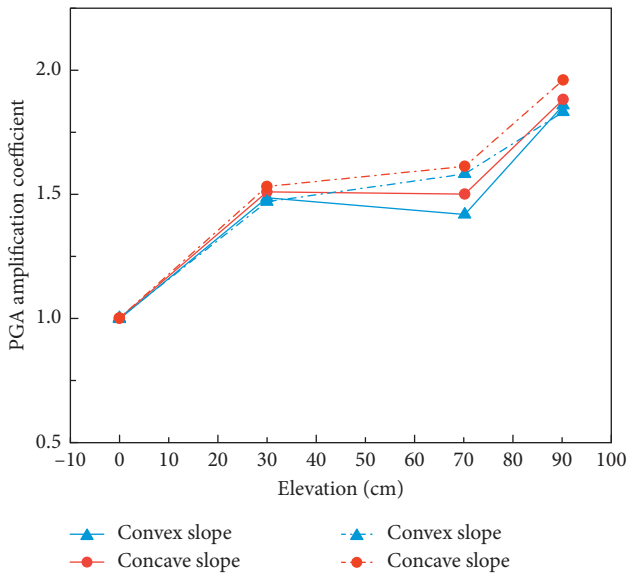

Figure 15: PGA amplification coefficients under condition ELC-1 and SIN-1.

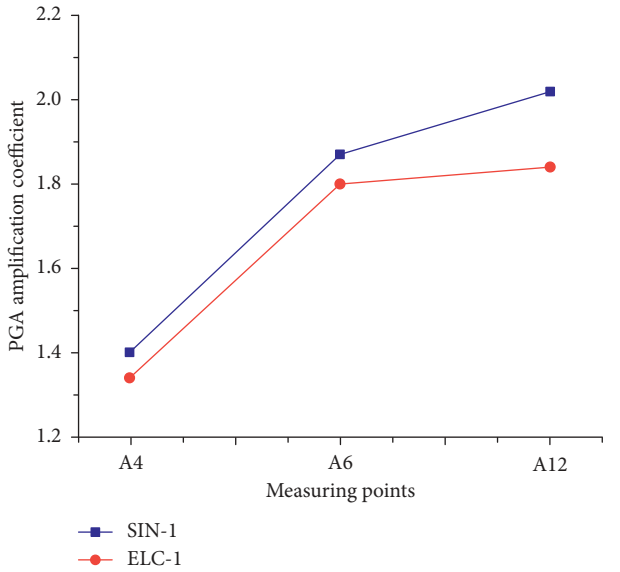

Figure 16: Comparison of PGA amplification coefficients under varying seismic waves.

coefficients of the convex slope surface showed a small fluctuation in the early stage and continued increasing before gradually decreasing. Amplification coefficients measured inside the concave slope increased gradually from 0.1 g to 0.3 g, and A13 increased the most. In the later period, PGA amplification coefficients decreased gradually, and A1 declined most remarkably. All measuring points on the slope showed the above characteristics; that is, with an increase in ground motion amplitudes, PGA amplification coefficients exhibited an initial increase followed by a stable stage and ultimate decline. The greater the acceleration amplitudes, the higher the dynamic stress level; therefore, the shear modulus declined while the damping ratio increased, and

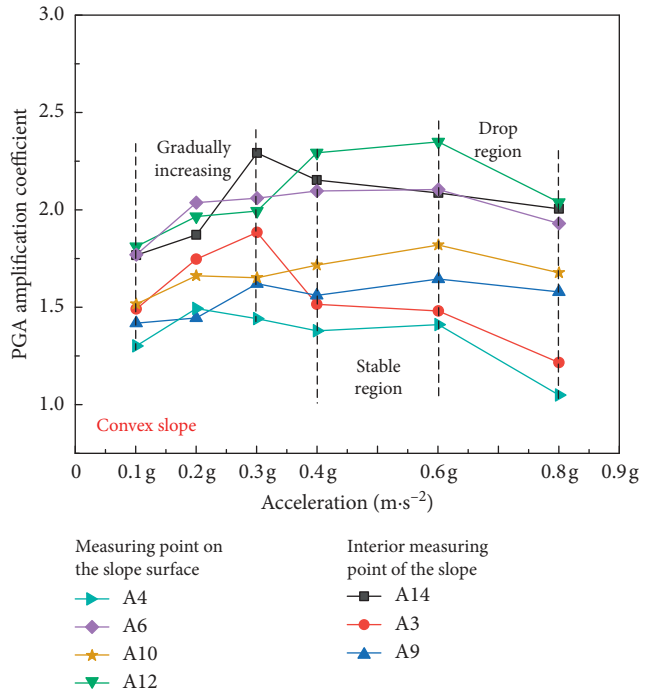

Figure 17: PGA amplification coefficients of convex slope under different El Centro waves.

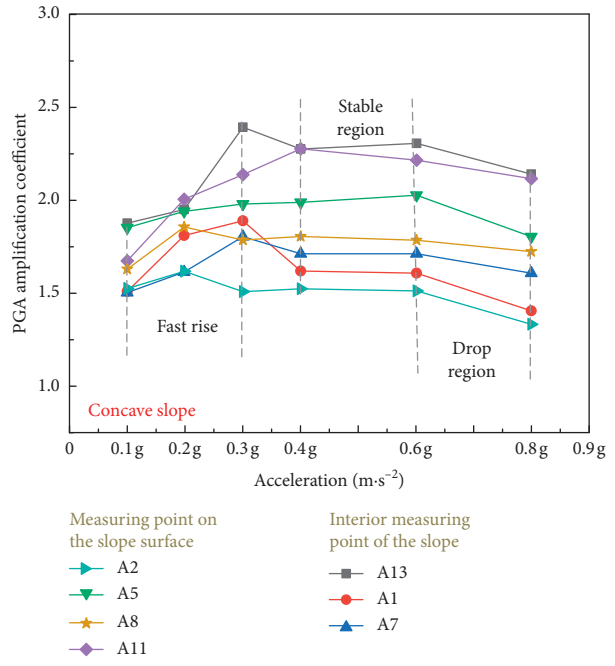

Figure 18: PGA amplification coefficients of concave slope under different El Centro wave.

the vibration-insulating effect on earthquake waves of the slope strengthened.

Figure 19 presents the variation law of PGA amplification coefficients along elevation under SIN-1 and SIN-5. Findings show that PGA amplification coefficients measured inside the slope and on the slope surface generally increased,

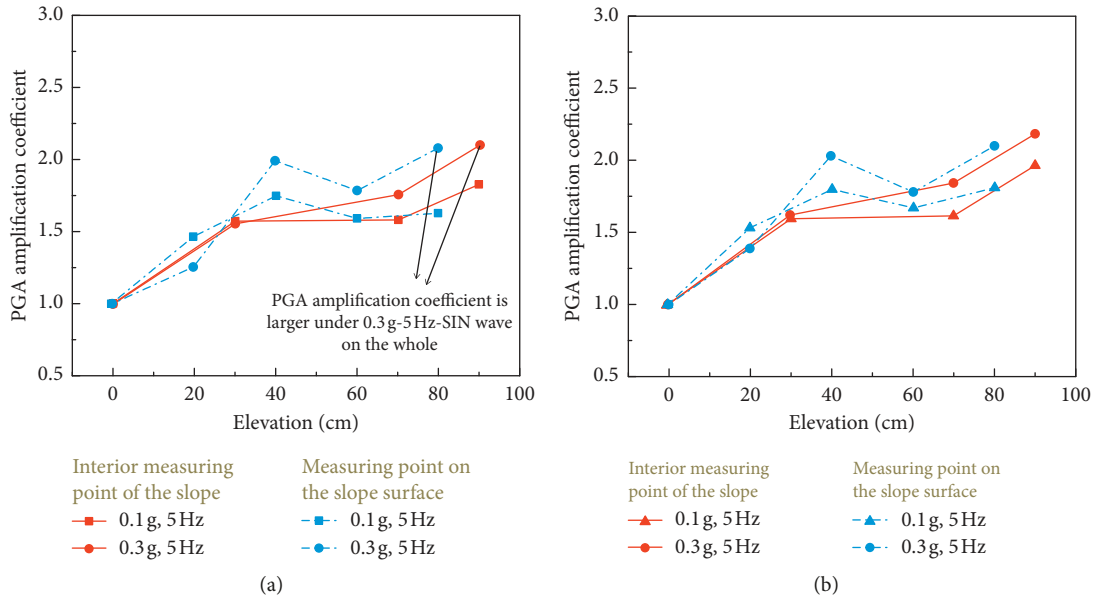

Figure 19: (a) PGA amplification coefficients of convex slope under different sine waves. (b) PGA amplification coefficients of concave slope under different sine waves.

whereas coefficients measured on the slope surface declined near the slope line. PGA amplification coefficients under 0.3 g acceleration amplitude were larger than those under 0.1 g, indicating that the vibration intensity had a significant effect on acceleration amplification. Yet the curves of the two conditions were mostly consistent, implying that vibration intensity exerted little effect on the dynamic response distribution of the slope along the elevation. These results reveal that the distribution law of PGA amplification coefficients of the slope was similar under different seismic loads. Vibration intensity had little effect on the dynamic response law of the slope along elevation, but it had a clear influence on the acceleration magnification effect.

According to the principle of seismic dynamics, when the load frequency is the same as the natural frequency of the slope, the slope will exhibit resonance. Natural frequencies of our model were determined according to Fourier spectrum analysis. A self-vibration test of the model box was conducted before the test, providing a basis for the reasonable selection of test frequency. The loading scheme was designed for the sine wave frequency at 5, 7.5, 10, and 12.5 Hz to analyze the effect of frequency on the dynamic response of the slope.

Figure 20(a) presents the curve of the PGA amplification coefficient of the convex slope at various frequencies under different sine waves at 0.1 g acceleration amplitude. With an increase in frequency, the PGA amplification coefficients measured on A9 and A14 showed an upward trend, whereas that of A3 remained stable first and then declined sharply. The PGA amplification coefficients of A4 and A12 on the slope surface retained an initial slight upward tendency followed by a sharp decline. The PGA amplification coefficients of A6 and A10 exhibited an upward trend along the elevation; the growth was rapid and then slowed. Figure 20(b) shows the curve of PGA amplification coefficients of the concave slope with different frequencies under sine waves with 0.1 g acceleration amplitude. The PGA amplification coefficients measured in the concave slope rose with an increase in frequency. The coefficients measured on A2 and A11 exhibited a slow growth trend, and those on A5 and A8 demonstrated a generally upward trend with a slight decline around 10 Hz.

6. Dynamic Failure Modes

6.1. Phenomenon of Dynamic Damage. This section describes the dynamic failure process of the model slope under seismic loading. The concave slope showed no obvious deformation phenomena under the first few working conditions. Figure 21(a) shows a slight slip of the upper slope under condition SIN-5.

Figure 21(b) reveals that from working conditions SIN-6 to SIN-7, cracks in the model slope developed further. Cracks appeared on both sides of the slope shoulder under SIN-6. Under ELC-6 and ELC-7 conditions, a 5 cm long crack appeared on the top of the slope, extending from the back of the model to the slope surface at a 45-degree angle, and slight dislocation occurred at the interface of the muddy interlayer.

From conditions SIN-8 to SIN-9 (Figure 21(c)), the slope crevices ran through the lower part of the slope line to form a slip surface, and the upper slope sheared along the muddy interface to the free surface with bulges in the slope toe before the whole slope was destroyed.

For the convex slope, under the first few working conditions, no obvious damage was observed. When loading SIN-6, cracks appeared in the upper part of the shoulder, extending from the edge of the slope to the inner part of the slope; cracks also appeared at the interface of the weak interlayer. Under condition ELC-7, cracks in the layered

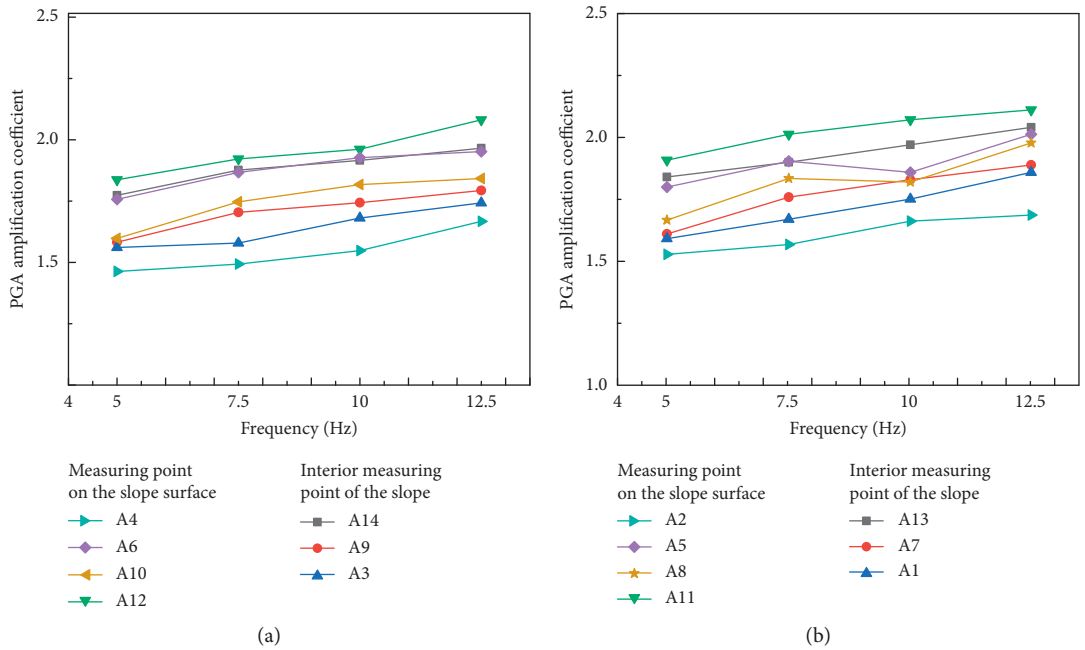

Figure 20: (a) PGA amplification coefficients of convex slope under sine waves with different frequencies. (b) PGA amplification coefficients of concave slope under sine waves with different frequencies.

Figure 21: Continued.

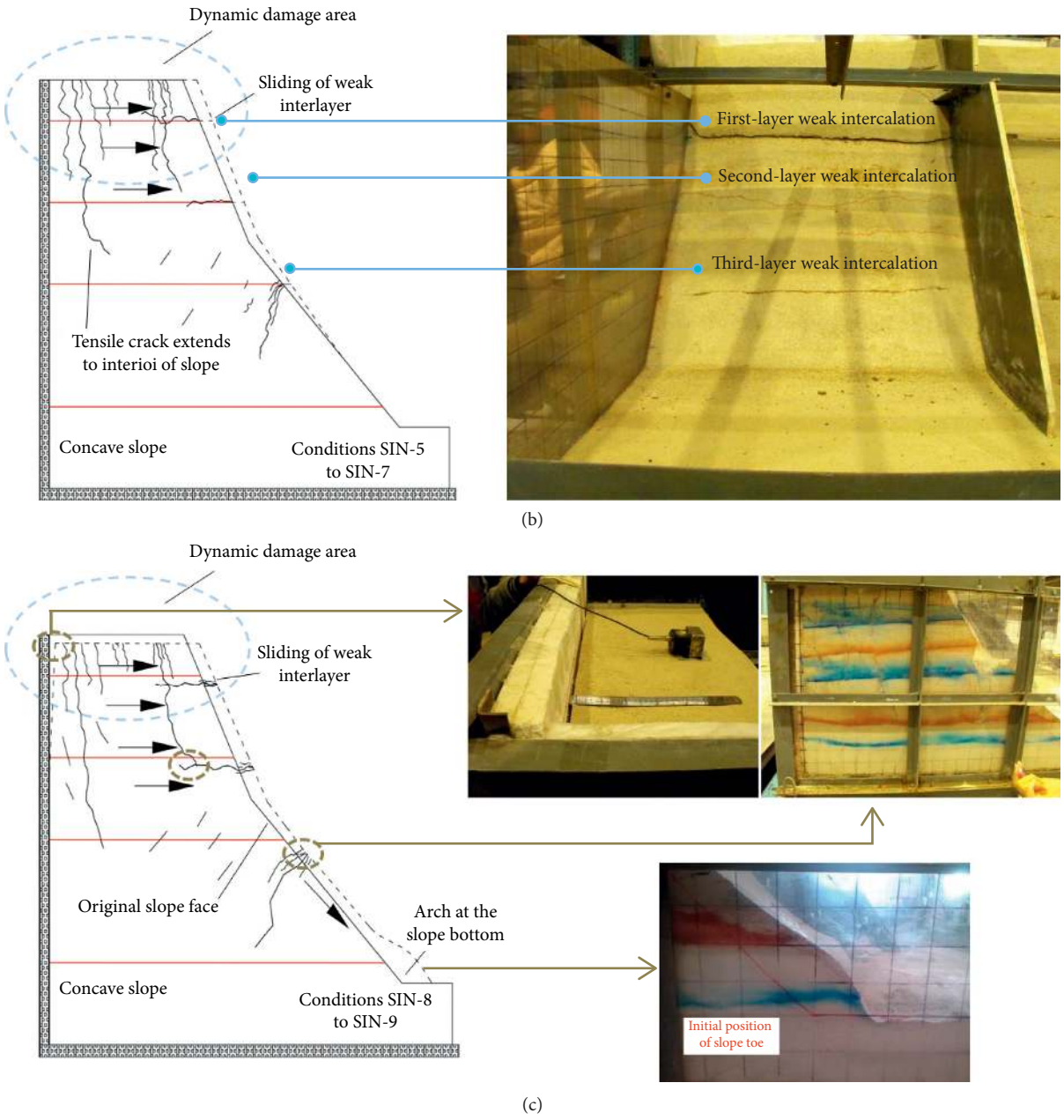

Figure 21: Illustration of the breakage process of concave slope under seismic loading. (a) First stage of model failure. (b) Second stage of model failure. (c) Third stage of model failure.

interface widened further. Local collapse occurred in the middle of the second and third muddy intercalations near the slope line under SIN-8. Under SIN-9, a collapse occurred near the slope line, and interlayer dislocation was obvious; the model slope was ultimately destroyed. According to failure phenomena observed in the test, the dynamic failure process of the convex slopes is illustrated in Figure 22.

Results indicate that dynamic failure of the concave slope mainly manifested by sliding and collapse of the slope along the sliding surface and shear sliding of the weak interlayer. Tensile cracks were produced on the top of the slope and extended with an increase in amplitude, forming a thorough slip surface. Then, the slope shoulder slid out and led to slope failure. The dynamic failure modes of the concave slope included collapse of the whole slope near the slope line under strong earthquake conditions and shear sliding along the weak interlayer. At the same time, longitudinal cracks in the slope connected with horizontal cracks, leading to model destruction.

6.2. Influence Factors of Slope Deformation and Failure. By observing the deformation and failure phenomena of different slope types during the test, the influences of diverse factors on slope deformation and failure under seismic load were revealed. These factors mainly included slope shape,

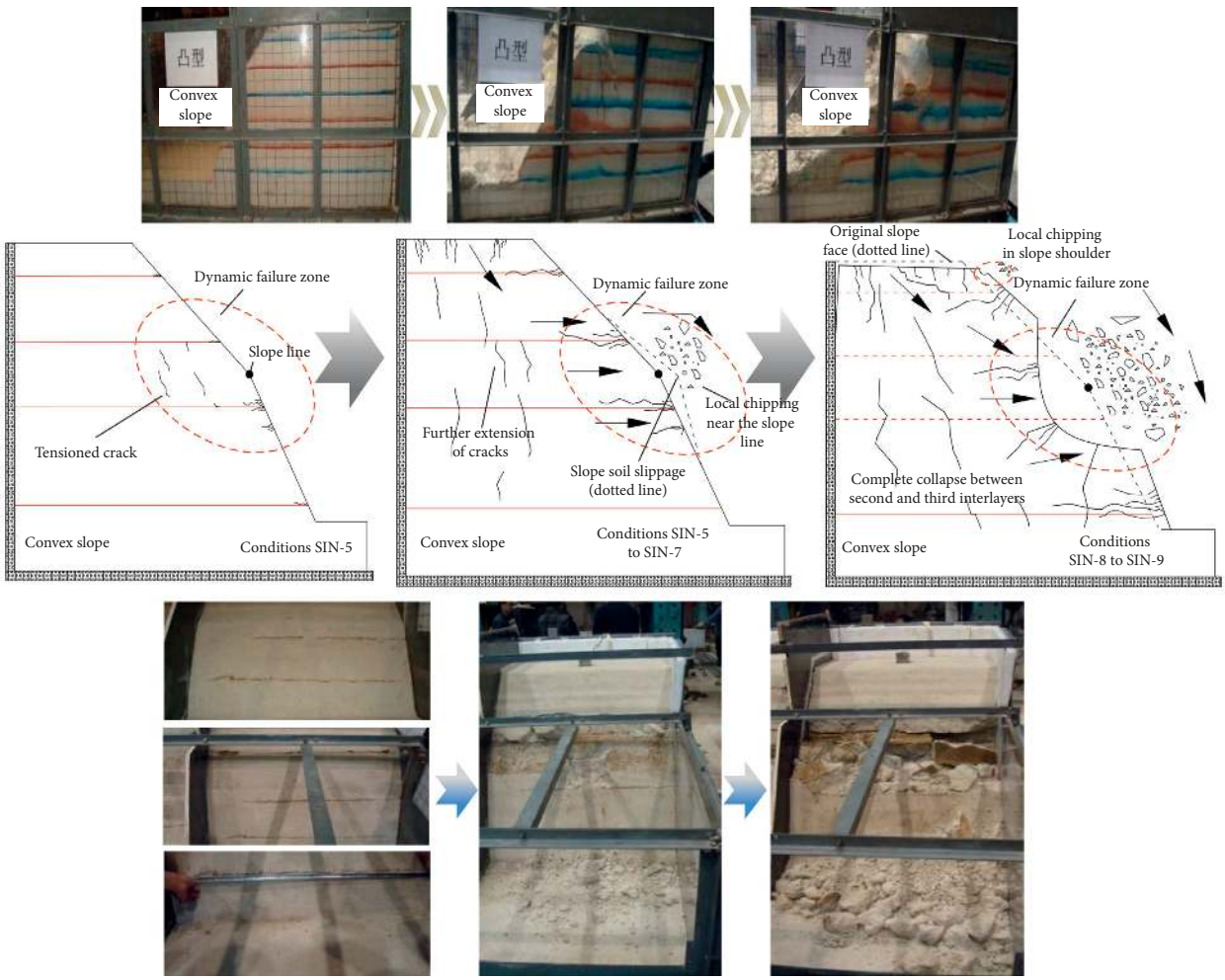

Figure 22: Illustration of the breakage process of convex slope under seismic loading.

slope structure, and seismic load conditions. The observation demonstrated two modes of deformation and failure for the concave and convex slopes. The concave slope demonstrated an obvious collapse in the upper part of the slope line, and large cracks appeared in the slope body; then, the slope toe bulged. The convex slope collapsed near the slope line, and many interlaced cracks appeared inside the slope. The overall stability of the convex slope was thus stronger than that of the concave slope under seismic load, and the concave slope was more sensitive to the acceleration dynamic response than the convex slope. Moreover, slippage occurred in varying degrees at the interface of the four mud layers, with clearer slippage at the upper part of the slope than at the lower part. On one hand, the effect of elevation amplification was remarkable; on the other, muddy interlayers comprised the weak area of the slope. These areas were subject to seismic loads, which could easily induce overall slope failure.

The influences of seismic load conditions on slope failure were primarily reflected in amplitude and duration. Under the first few working conditions with relatively small amplitudes, the amplitude and duration exerted little effect on the model with nearly no deformation. With an increase in amplitude and duration, the dynamic response of the slope model increased, and cracks and slips appeared. The cracks extended and expanded until the model was destroyed. The stronger the vibration intensity of the seismic waves on the slope, the greater the seismic inertia force and the more damage to the slope. The total energy of ground motion input into the slope increased with an increase in duration, leading to accumulating slope damage. Under continuous loading, slope deformation became increasingly large, and slope displacement rose continuously, eventually resulting in slope failure. When the ground motion parameters were identical, the destructive force of the sine wave on the slope model was notably stronger than that of the El Centro wave [48, 49].

7. Conclusions

Through a shaking table test, the failure modes and dynamic response law of a high slope were studied. Based on test data, the effects of landform, slope type, elevation, and ground motion parameters on dynamic response of the slope were analyzed in depth. The following conclusions were drawn:

(1) The differences in PGA amplification coefficients between symmetrically measured points on the

convex and concave slopes were not overly large. PGA amplification coefficients of the concave slope were slightly larger than those of the convex slope. Slope type influenced the acceleration response; the convex slope was more stable than the concave slope. Coefficients measured on the slope surface were always greater than those inside the slope. The PGA amplification coefficients measured inside the slope and on the slope surface increased by line, exhibiting nonlinear characteristics.

(2) Seismic wave type had a significant influence on dynamic response of the slope. The spectrum characteristics of different seismic waves varied greatly, leading to different acceleration amplification effects. Under the same conditions, the acceleration amplification effect of the sine wave was more significant than that of the El Centro wave. With an increase in seismic amplitude, PGA amplification coefficients increased initially followed by a stable stage and later declined. With an increase in frequency, the dynamic response of acceleration presented a nonlinear change. The dynamic amplification effect of the slope was closely related to the natural frequency. Within a certain range, the higher the frequency, the more significant the amplification effect.

(3) Different slope types introduced diverse failure modes, destruction positions, and degrees of failure. The concave slope was dominated by shoulder collapse, whereas the convex slope primarily collapsed near the slope line. Structural characteristics of the slope controlled slope deformation and failure. The position of the muddy interlayer was weak and prone to collapsing and slipping, which reduced slope stability.

(4) Higher vibration intensity induced greater slope deformation and failure. The duration was closely related to the total energy input by ground motion. The duration increased and ground motion energy accumulated continuously, resulting in continuous accumulation of slope damage and ultimate instability.

Data Availability

The data used to support the findings of this study are available from the corresponding author upon request.

Conflicts of Interest

The authors declare that there are no conflicts of interest regarding the publication of this paper.

Acknowledgments

This work was financially supported by the National Key R&D Program of China (no. 2018YFC0808706).

References

[1] D. Pradel, P. M. Smith, J. P. Stewart, and G. Raad, "Case history of landslide movement during the Northridge earthquake," *Journal of Geotechnical and Geoenvironmental Engineering*, vol. 131, no. 11, pp. 1360–1369, 2005.

[2] X. L. Luo, D. Y. Li, Y. Yang, and S. R. Zhang, "Spatiotemporal Traffic Flow Prediction with KNN and LSTM," *Journal of Advanced Transportation*, vol. 2019, Article ID 4145353, 12 pages, 2019.

[3] J. Wasowski, D. K. Keefer, and C. T. Lee, "Toward the next generation of research on earthquake-induced landslides: current issues and future challenges," *Engineering Geology*, vol. 122, no. 1-2, pp. 1–8, 2011.

[4] J. Qiu, X. Wang, S. He, H. Liu, J. Lai, and L. Wang, "The catastrophic landside in maoxian county, sichuan, SW China, on June 24, 2017," *Natural Hazards*, vol. 89, no. 3, pp. 1485–1493, 2017.

[5] R. Q. Huang and W. L. Li, "Analysis of the geo-hazards triggered by the 12 may 2008 Wenchuan earthquake, China," *Bulletin of Engineering Geology and the Environment*, vol. 68, no. 3, pp. 363–371, 2009.

[6] F. C. Dai, C. Xu, X. Yao, L. Xu, X. B. Tu, and Q. M. Gong, "Spatial distribution of landslides triggered by the 2008 Ms 8.0 Wenchuan earthquake, China," *Journal of Asian Earth Sciences*, vol. 40, no. 4, pp. 883–895, 2011.

[7] J. Lai, S. He, J. Qiu et al., "Characteristics of seismic disasters and aseismic measures of tunnels in Wenchuan earthquake," *Environmental Earth Sciences*, vol. 76, no. 2, 2017.

[8] S. Zhang, L. M. Zhang, and T. Glade, "Characteristics of earthquake- and rain-induced landslides near the epicenter of Wenchuan earthquake," *Engineering Geology*, vol. 175, no. 11, pp. 58–73, 2014.

[9] C. Xu and X. Xu, "Statistical analysis of landslides caused by the Mw 6.9 Yushu, China, earthquake of April 14, 2010," *Natural Hazards*, vol. 72, no. 2, pp. 871–893, 2014.

[10] C. Xu, X. Xu, J. B. H. Shyu, W. Zheng, and W. Min, "Landslides triggered by the 22 July 2013 Minxian-Zhangxian, China, Mw 5.9 earthquake: inventory compiling and spatial distribution analysis," *Journal of Asian Earth Sciences*, vol. 92, pp. 125–142, 2014.

[11] M. Garevski, Z. Zugic, and V. Sesov, "Advanced seismic slope stability analysis," *Landslides*, vol. 10, no. 6, pp. 729–736, 2013.

[12] C. H. Zhang, O. A. Pekau, F. Jin, and W. Guanglun, "Application of distinct element method in dynamic analysis of high rock slope and blocky structures," *Soil Dynamics and Earthquake Engineering*, vol. 16, no. 6, pp. 385–394, 1997.

[13] Z. J. Zhou, S. S. Zhu, X. Kong, J. T. Lei, and T. Liu, "Optimization analysis of settlement parameters for post-grouting piles in loess area of Shaanxi, China," *Advances in Civil Engineering*, vol. 2019, Article ID 7085104, 11 pages, 2019.

[14] G. D. Bouckovalas and A. G. Papadimitriou, "Numerical evaluation of slope topography effects on seismic ground motion," *Soil Dynamics and Earthquake Engineering*, vol. 25, no. 7-10, pp. 547–558, 2005.

[15] Y. Li, S. Xu, H. Liu, E. Ma, and L. Wang, "Displacement and stress characteristics of tunnel foundation in collapsible loess ground reinforced by jet grouting columns," *Advances in Civil Engineering*, vol. 2018, Article ID 2352174, 16 pages, 2018.

[16] K. Toki, F. Miura, and Y. Oguni, "Dynamic slope stability analyses with a non-linear finite element method," *Earthquake Engineering & Structural Dynamics*, vol. 13, no. 2, pp. 151–171, 1985.

[17] M. Jiang, T. Jiang, G. B. Crosta, Z. Shi, H. Chen, and N. Zhang, "Modeling failure of jointed rock slope with two main joint sets using a novel DEM bond contact model," *Engineering Geology*, vol. 193, pp. 79–96, 2015.

[18] G. Fan, J. Zhang, J. Wu, and K. Yan, "Dynamic response and dynamic failure mode of a weak intercalated rock slope using a shaking table," *Rock Mechanics and Rock Engineering*, vol. 49, no. 8, pp. 3243–3256, 2016.

[19] Y. W. Zhang, X. L. Weng, Z. P. Song, and Y. F. Sun, "Modeling of loess soaking induced impacts on metro tunnel using water soaking system in centrifuge," *Geofluids*, vol. 2019, Article ID 5487952, 13 pages, 2019.

[20] H. Yu, X. Yan, A. Bobet, Y. Yuan, G. Xu, and Q. Su, "Multi-point shaking table test of a long tunnel subjected to non-uniform seismic loadings," *Bulletin of Earthquake Engineering*, vol. 16, no. 2, pp. 1041–1059, 2018.

[21] R. W. Clough and D. Pirtz, "Earthquake resistance of rock-fill dams," *Journal of the Soil Mechanics and Foundations Division*, vol. 82, no. 2, pp. 1–26, 1956.

[22] S. J. Wang and J. M. Zhang, "On the dynamic stability of block sliding on rock slopes," *Scientia Geologica Sinica*, vol. 2, pp. 162–170, 1982.

[23] K. L. Wang and M. L. Lin, "Initiation and displacement of landslide induced by earthquake: a study of shaking table model slope test," *Engineering Geology*, vol. 122, no. 1-2, pp. 106–114, 2011.

[24] C. Yang, J. Zhang, F. Liu, J. Bi, and Z. Jun, "Analysis on two typical landslide hazard phenomena in the Wenchuan earthquake by field investigations and shaking table tests," *International Journal of Environmental Research and Public Health*, vol. 12, no. 8, pp. 9181–9198, 2015.

[25] M. Zhao, D. Huang, M. Cao et al., "Shaking table tests on deformation and failure mechanisms of seismic slope," *Journal of Vibro Engineering*, vol. 17, no. 1, pp. 382–392, 2015.

[26] O. Matsuo, K. Yokoyama, and Y. Saito, "Shaking table tests and analyses of geosynthetic-reinforced soil retaining walls," *Geosynthetics International*, vol. 5, no. 1-2, pp. 97–126, 1998.

[27] G. Xu, L. Yao, Z. Gao, and C. Li, "Large-scale shaking table model test study on dynamic characteristics and dynamic response of slope," *Chinese Journal of Rock Mechanics and Engineering*, vol. 27, no. 3, pp. 624–632, 2008.

[28] T. Yang, T. Xu, H. Liu et al., "Rheological characteristics of weak rock mass and effects on the long-term stability of slopes," *Rock Mechanics and Rock Engineering*, vol. 47, no. 6, pp. 2253–2263, 2014.

[29] A. Che, H. Yang, B. Wang, and X. Ge, "Wave propagations through jointed rock masses and their effects on the stability of slopes," *Engineering Geology*, vol. 201, no. 2, pp. 45–56, 2016.

[30] C. J. Lee, Y. C. Wei, and Y. C. Kuo, "Boundary effects of a laminar container in centrifuge shaking table tests," *Soil Dynamics and Earthquake Engineering*, vol. 34, no. 1, pp. 37–51, 2012.

[31] T. Kokusho and T. Ishizawa, "Energy approach for earthquake induced slope failure evaluation," *Soil Dynamics and Earthquake Engineering*, vol. 26, no. 2–4, pp. 221–230, 2006.

[32] H. I. Ling, Y. Mohri, D. Leshchinsky, C. Burke, K. Matsushima, and H. Liu, "Large-scale shaking table tests on modular-block reinforced soil retaining walls," *Journal of Geotechnical and Geoenvironmental Engineering*, vol. 131, no. 4, pp. 465–476, 2005.

[33] J. Wartman, R. B. Seed, and J. D. Bray, "Shaking table modeling of seismically induced deformations in slopes," *Journal of Geotechnical and Geoenvironmental Engineering*, vol. 131, no. 5, pp. 610–622, 2005.

[34] M. L. Lin and K. L. Wang, "Seismic slope behavior in a large-scale shaking table model test," *Engineering Geology*, vol. 86, no. 2-3, pp. 118–133, 2006.

[35] H. Liu, Q. Xu, Y. Li, and X. Fan, "Response of high-strength rock slope to seismic waves in a shaking table test," *Bulletin of the Seismological Society of America*, vol. 103, no. 6, pp. 3012–3025, 2013.

[36] H. X. Liu, Q. Xu, and Y. R. Li, "Effect of lithology and structure on seismic response of steep slope in a shaking table test," *Journal of Mountain Science*, vol. 11, no. 2, pp. 371–383, 2014.

[37] E. Buckingham, "On physically similar systems; illustrations of the use of dimensional equations," *Physical Review*, vol. 4, no. 4, pp. 345–376, 1914.

[38] L. Brand, "The Pi theorem of dimensional analysis," *Archive for Rational Mechanics and Analysis*, vol. 1, no. 1, pp. 35–45, 1957.

[39] W. D. Curtis, J. D. Logan, and W. A. Parker, "Dimensional analysis and the pi theorem," *Linear Algebra and Its Applications*, vol. 47, pp. 117–126, 1982.

[40] H. B. Havenith, M. Vanini, D. Jongmans, and E. Faccioli, "Initiation of earthquake-induced slope failure: influence of topographical and other site specific amplification effects," *Journal of Seismology*, vol. 7, no. 3, pp. 397–412, 2003.

[41] Q. Yan, Y. Xu, W. Zhang, P. Geng, and W. Yang, "Numerical analysis of the cracking and failure behaviors of segmental lining structure of an underwater shield tunnel subjected to a derailed high-speed train impact," *Tunnelling and Underground Space Technology*, vol. 72, pp. 41–54, 2018.

[42] S. Iai, "Similitude for shaking table tests on soil-structure-fluid model in 1g gravitational field," *Soils and Foundations*, vol. 29, no. 1, pp. 105–118, 1989.

[43] J. Lai, K. Wang, J. Qiu, F. Niu, J. Wang, and J. Chen, "Vibration response characteristics of the cross tunnel structure," *Shock and Vibration*, vol. 2016, Article ID 9524206, 16 pages, 2016.

[44] Y. L. Lin and G. L. Yang, "Dynamic behavior of railway embankment slope subjected to seismic excitation," *Natural Hazards*, vol. 69, no. 1, pp. 219–235, 2013.

[45] Z. F. Wang, S. L. Shen, and G. Modoni, "Enhancing discharge of spoil to mitigate disturbance induced by horizontal jet grouting in clayey soil: theoretical model and application," *Computers and Geotechnics*, 2019, In press.

[46] J. Lai, S. Mao, J. Qiu et al., "Investigation progresses and applications of fractional derivative model in geotechnical engineering," *Mathematical Problems in Engineering*, vol. 2016, Article ID 9183296, 15 pages, 2016.

[47] Y. W. Zhang, Z. P. Song, X. L. Weng, and Y. L. Xie, "A new soil-water characteristic curve model for unsaturated loess based on wetting-induced pore deformation," *Geofluids*, vol. 2019, Article ID 5261985, 13 pages, 2019.

[48] X. Z. Li, X. L. Qu, C. Z. Qi, and Z. S. Shao, "A unified analytical method calculating brittle rocks deformation induced by crack growth," *International Journal of Rock Mechanics and Mining Sciences*, vol. 113, pp. 134–141, 2019.

[49] J. Lai, J. Qiu, H. Fan, Q. Zhang, J. Wang, and J. C. Hen, "Fiber bragg grating sensors-based in-situ monitoring and safety assessment of loess tunnel," *Journal of Sensors*, vol. 2016, Article ID 8658290, 10 pages, 2016.